J. Fluid Mech. (1989), *vol.* 207, *pp.* 453–474
Printed in Great Britain

Convection in a rotating cavity: modelling ocean circulation

By SCOTT A. CONDIE† AND ROSS W. GRIFFITHS
Research School of Earth Sciences, Australian National University, GPO Box 4, Canberra, ACT 2601, Australia

(Received 4 November 1988 and in revised form 3 April 1989)

Large-scale oceanic flows, ranging from large estuaries to basin-scale abyssal circulation, can be driven by imposed lateral density gradients and are significantly influenced by the Earth's rotation. Some essential features of such flows have been incorporated into a laboratory model by differentially heating and cooling the vertical endwalls of a shallow rectangular cavity, rotating about a vertical axis through its centre. In this paper, the flow observed after this system had been allowed to develop to a steady mean state is described. Measurements were made of the velocity and temperature fields, as well as the variability in temperature field associated with eddy motions. The temperature data were also used to calculate the potential vorticity distribution within the cavity. These results indicate that the heated and cooled end-walls acted not only as continuous sources of buoyancy, but also of anomalous potential vorticity. It is shown that the potential vorticity served as an indicator and tracer of the laboratory flow. The structure and location of boundary currents were largely determined by nonlinear potential vorticity dynamics which resulted in a mean circulation consisting of two basin-scale counter-rotating gyres. This flow differed markedly from the initial boundary currents set up by Kelvin waves.

1. Introduction

The problem of a shallow cavity with differentially heated and cooled endwalls has been studied extensively (for example Cormack, Leal & Imberger 1974; Imberger 1974; Simpkins & Dudderar 1981; Bejan, Al-Homoud & Imberger 1981). This configuration is relevant to convective processes in lakes and estuaries, as well as a diverse range of engineering applications. Furthermore, a study by Patterson (1984) in which the heating and cooling were replaced by a linear distribution (in the horizontal) of sources and sinks, exhibited similar regimes to the convective flow, suggesting that the latter system may be relevant to a broad range of buoyancy-driven flows. The present study considers the effects of rotating a cavity with differentially heated endwalls. With the addition of rotation, the flow becomes far more complex, but has features in common with large-scale thermohaline circulation within ocean basins and other large water bodies.

Attention is drawn to two related experiments involving both rotation and convection. Sugimoto & Whitehead (1983) studied convective flows in a shallow rectangular sea of constant depth which adjoined a deep ocean through a uniformly sloping bottom region. The observed flow included a number of gyres controlled by

---

† Present address: Department of Oceanography, Old Dominion University, Norfolk, VA 23529, USA.

the rotation rate and the topography. Speer & Whitehead (1989) modelled convection in an ocean with non-uniform heating at the surface using a rotating rectangular cavity with non-uniform heating from below. Over much of the parameter range studied, the flow was dominated by a cyclonic gyre in the upper layer and weaker anticyclonic motions near the bottom.

The transient flow in our rotating cavity configuration has been described by Condie & Ivey (1988) and Condie (1989). Immediately after the heating and cooling were applied at the two endwalls, buoyant fluid adjacent to the hot endwall rose vertically and was turned into the interior by the upper horizontal lid (with a corresponding downward flow at the cold end). Coriolis forces pushed these currents to the right (with anticlockwise rotation) to form density currents along opposite walls, as would be expected on the basis of Kelvin wave propagation. This flow was unstable to baroclinic instabilities, which broke to form eddies. At low rotation rates the waves were damped by Ekman-layer dissipation, while at higher rotation rates they broke backwards (towards the source of the intrusion) to form cyclonic eddies. If unimpeded by neighbouring eddies, anticyclones formed on the downstream side of the cyclonic eddies to produce dipolar eddy pairs. Condie (1989) examined the long-term evolution of the flow through to its final state. The coupling of the boundary current circulation with the eddy motions transferred heat and momentum throughout the fluid. The transient development of the flow field was described and the timescales for the development of the density field within the cavity determined.

In this paper a detailed account of the steady-state flow is presented. We begin §2 by describing the experimental equipment in more detail. Appropriate parameters which govern the dynamics of the steady flow are then defined. In §3 the flow is described qualitatively, followed by a discussion of the potential vorticity dynamics of the mean flow and the role of baroclinic Rossby waves. Sections 4 and 5 then examine the temperature structure, the potential vorticity field and the variability in temperature associated with the eddy field. Since potential vorticity is a dynamically important property as well as a conservative tracer for the flow, its usefulness in revealing the geometry and dynamics of the laboratory flow is investigated. The convective heat transfer is considered in §6. In §7 we discuss the relevance of the study to ocean circulation.

2. Description of experiments

The basic experimental configuration is shown in figure 1. The convection tank consisted of a rectangular Perspex cavity of height $H = 15$ cm, length $L = 200$ cm and width $B = 60$ cm. Heat exchangers formed the two vertical endwalls of the tank. These were constructed from a 3.0 cm thick aluminium block which had 1.2 cm square grooves through which heated or cooled water flowed. To ensure an even temperature distribution over the heat exchanger surface, a 1.0 cm thick block of copper was in contact with the working fluid. Thermistors embedded in the copper and aluminium plates allowed both the temperature in contact with the fluid and the heat flux into the working fluid to be measured. The base and sides of the cavity were insulated with 10 cm thick expanded polystyrene. The lid was designed as a series of sealed transparent air cavities, and when visual access was not required a further 10 cm of polystyrene was fitted. This assembly was mounted on a rotating table, incorporating fluid slip rings to allow the hot and cold baths supplying fluid to the endwalls to be located off the table. There were also active thermistor bridges on the turntable for amplification of thermistor probe signals. The amplified signals passed

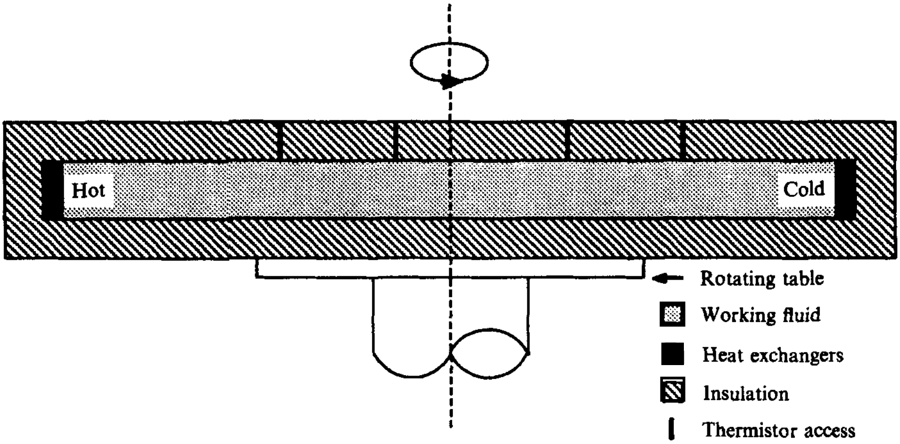

FIGURE 1. A side view of the experimental apparatus, consisting of the insulated convection tank resting on the rotating table.

through electrical connections from the rotating to the stationary reference frame where they were recorded.

The dynamics of the flows produced in the rotating cavity configuration are determined by five independent non-dimensional parameters (Condie 1989). These are the aspect ratio

$$A = \frac{H}{L}, \tag{1}$$

the Prandtl number

$$Pr = \frac{\nu}{\kappa}, \tag{2}$$

the Rayleigh number

$$Ra = \frac{g\alpha\Delta T H^3}{\nu\kappa}, \tag{3}$$

the Ekman number

$$Ek = \frac{\nu}{H^2 f}, \tag{4}$$

and a rotating Froude number

$$Fr = \frac{B^2 f^2}{g\alpha\Delta T H}. \tag{5}$$

Here ν is the kinematic viscosity, κ is the thermal diffusivity, α is the coefficient of thermal expansion, ΔT is the temperature difference between the endwalls and f is the Coriolis parameter. Note that Ek is the square of the ratio of the Ekman-layer depth to the total depth, while Fr is the square of the ratio of the cavity width to the Rossby deformation radius.

For each experimental run the tank was filled with water and spun-up to solid-body rotation. Heating and cooling were then applied to the two endwalls and the system allowed to come to a steady mean state (~ 10 hours). The flow was visualized by introducing dye at the centre of the heated (or cooled) endwall. In other runs (to be described in §4), the temperature field was investigated by vertically traversing a rack of 15 fast response thermistors which were equally spaced across the width of the tank. This procedure was used to measure temperature sections at four positions along the length of the tank.

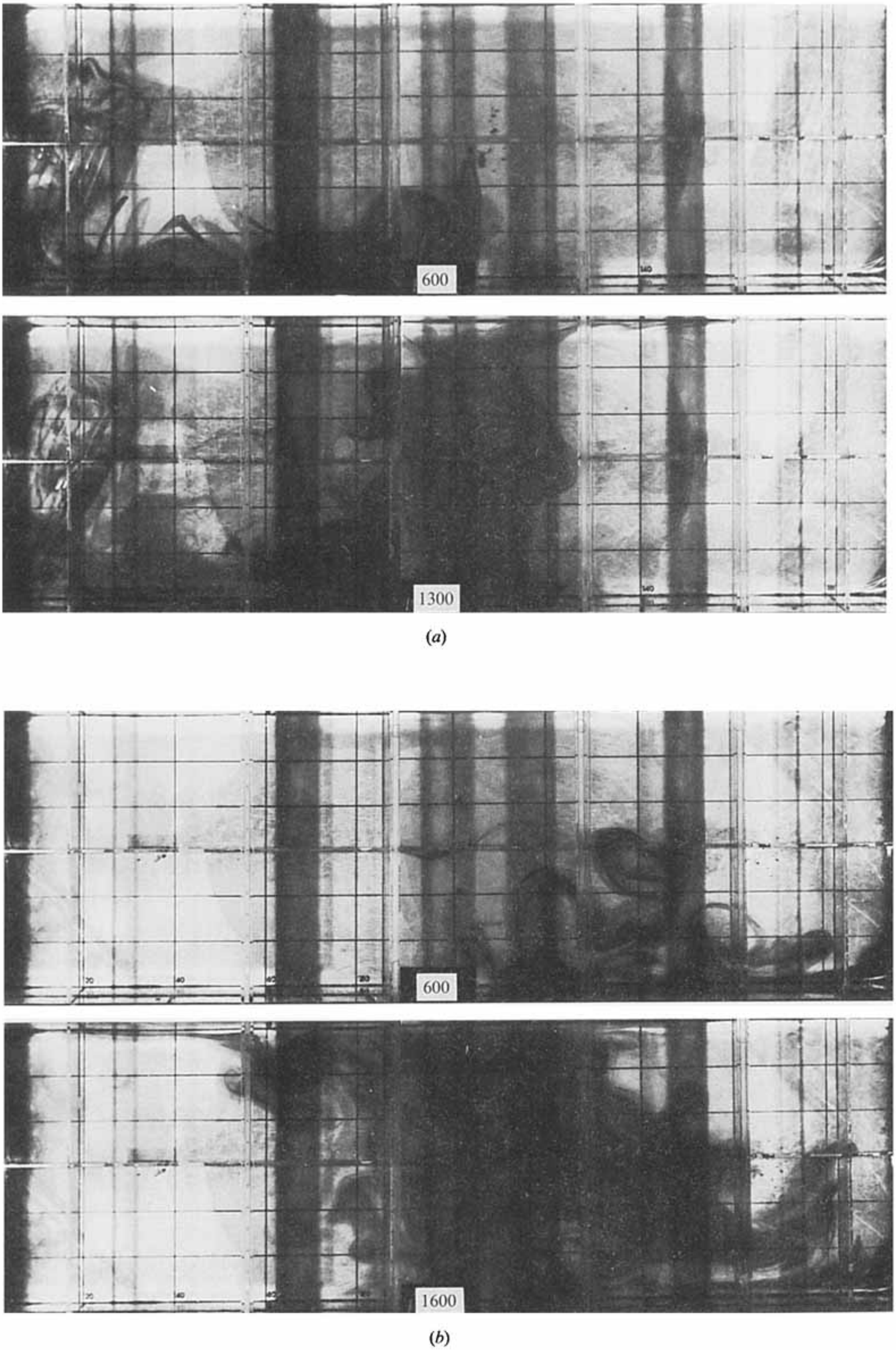
600
1300
(a)
600
1600
(b)

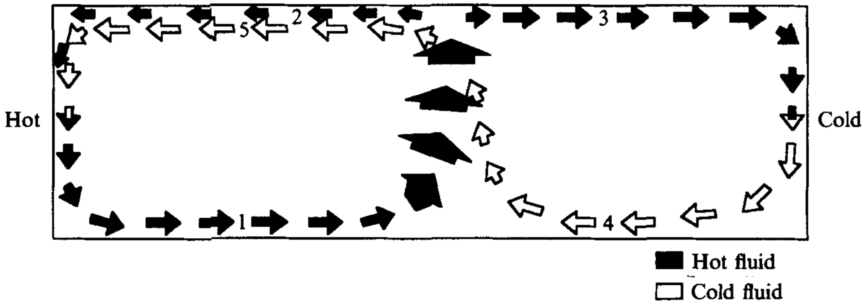

FIGURE 3. A pictorial representation of the mean flow observed in the cavity when $Ek < 10^{-4}$. The main boundary currents are numbered for later reference.

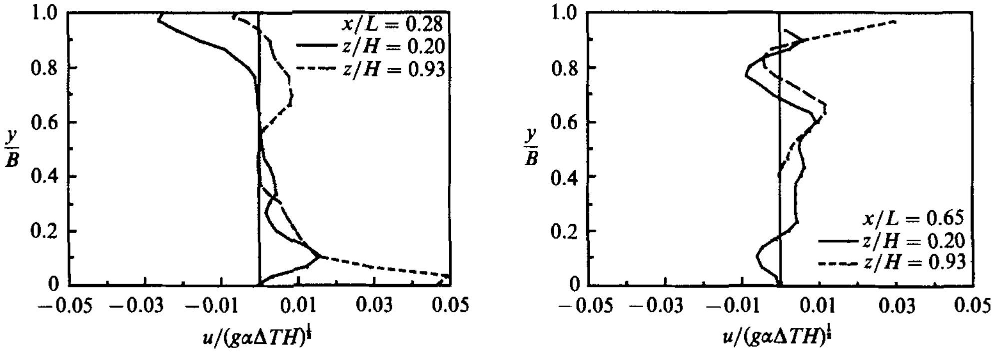

FIGURE 4. Cross-stream velocity profiles recorded at two depths (z is measured from the bottom) and two positions along the cavities length (x is measured from the heated endwall) when $Ra = 8.7 \times 10^8$, $Ek = 4.5 \times 10^{-5}$ and $Fr = 65$. The velocity is non-dimensionalized by the forcing term $(g\alpha \Delta TH)^{\frac{1}{2}}$.

3. Investigation of the mean flow

The photographs in figures 2(*a*) and 2(*b*) show the dyed flow which originated from the hot and cold endwalls respectively, when the Froude number was large and the Ekman number small. Eddies were prominent features under these conditions; however, in this section we shall concentrate on the mean flow in the cavity. After emerging from the thermal boundary layer, heated fluid travelled with the boundary on its right, as might be expected for anticlockwise rotation (figure 3). This boundary current became very weak in the second half of the cavity, with most of the warm fluid transported laterally across the central region of the tank in a diffuse cloud. Where the warm flow reached the opposite sidewall it broke into two narrow boundary jets, one of which returned to the hot end, while the other progressed towards the cold endwall. The latter was the stronger of the two jets and carried fluid in an anticyclonic motion around the perimeter of the cooled end of the tank.

As the warm fluid travelled along the cold endwall, it cooled and sank. On reaching

---

FIGURE 2. A plan view of the flow originating from (*a*) the hot end (on the right of the figure) and (*b*) the cold end (on the left of the figure) when $Ra = 2.2 \times 10^9$, $Ek = 2.4 \times 10^{-5}$ and $Fr = 71$ ($\Delta T = 24$ °C and $f = 1.5$). The number of rotation periods since dye began to be introduced is displayed at the bottom of the figure. The tank rotation is anticlockwise. In each case the dye is advected from the end to the centre of the tank and there crosses over to the opposite sidewall.

the right-hand (still looking from the hot to the cold end) side boundary it (surprisingly) formed a boundary current along the bottom of the wall (figure 2*b*). After progressing approximately halfway along the right-hand wall, this cold current meandered across to the opposite wall and continued to the heated endwall. These observations were supported by both instantaneous cross-stream velocity profiles obtained using the thymol-blue technique (figure 4) and temperature data to be presented in §4. The mean flow can therefore be described as consisting of two basin-scale gyres, as shown schematically in figure 3. The same basic flow pattern was also observed when the width of the cavity was reduced from $B = 60$ cm to $B = 15$ cm (by inserting an insulated divider along the length of the cavity).

The formation of the two large-scale gyres was an unexpected feature of the mean flow pattern. Kelvin wave dynamics on an f-plane suggest that a single cyclonic gyre should develop, with warm and cold boundary currents on either side of the cavity. The warm current flowing towards the cooled endwall (current 3 in figure 3) and the cold bottom current flowing away from that end (current 4) are both contrary to the direction of propagation of Kelvin waves. The asymmetry between the warm and cold flows suggested that the driving mechanism for the gyres may have been related to nonlinearity in the equation of state of water. Since the coefficient of thermal expansion α increases with temperature, the buoyancy flux which originated from the heated end was larger (by a factor of approximately two for $Ra = 2 \times 10^9$) than that from the cooled end, while the heat fluxes were equal. This difference led to a significantly stronger warm current at high Rayleigh numbers. This may explain the return flow of warm fluid (current 2 in figure 3) to the heated endwall: since all the heated fluid could not be pumped through the cold thermal boundary layer, a buildup of warm fluid may have reduced the alongshore pressure gradient sufficiently to allow the return flow. This mechanism accounts for the persistent and reproducible asymmetry between flow at opposite ends of the cavity. The existence of two gyres however, requires another explanation.

The cause of the observed two-gyre circulation is thought to be centrifugal effects, which imposed a paraboloidal shape on the isotherms. If we neglect the cross-stream parabolic variation and other distortions associated with the flow itself, then the isotherms form parabolas described by $\eta - \eta_0 = f^2(x-\frac{1}{2}L)^2/8g$, where η_0 is the height of the isotherm at the axis of rotation. The slope of potentials relative to the top and bottom of the tank is therefore

$$\frac{\partial \eta}{\partial x} = \frac{f^2(x-\frac{1}{2}L)}{4g}. \tag{6}$$

This could have affected the flow in the manner illustrated schematically in figure 5. Fluid originating from the heated end and travelling between isopycnal surfaces close to the lid tends to be stretched in the vertical. Conservation of potential vorticity then requires production of cyclonic relative vorticity. After this fluid passes the centre of rotation it is compressed, with a corresponding production of anticyclonic vorticity. Rather than continue along the right-hand wall, the warm water follows the path of least vorticity stretching, which takes it across the centre of the cavity. On reaching the opposite boundary it then breaks into two inertial jets (currents 2 and 3 in figure 3). A similar cycle, involving vertical compression followed by stretching of fluid near the base of the cavity, may account for the path of the cold water.

The ideas outlined in the previous paragraph were verified experimentally as follows. Equation (6) indicates that the position along the cavity where the bottom

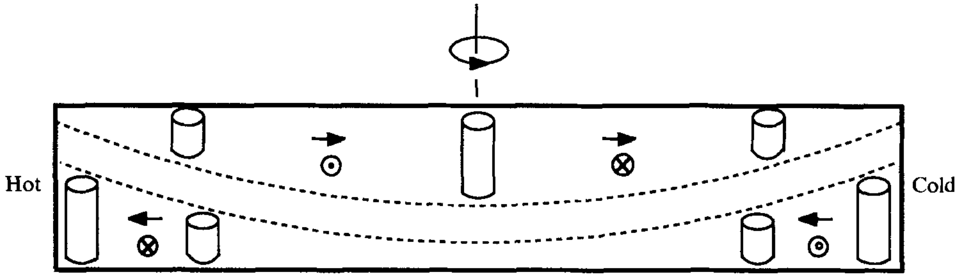

FIGURE 5. Schematic representation of the effects of parabolic-shaped isopotentials on fluid columns. Arrows represent the direction of flow parallel with the page, while ⊙ and ⊗ indicate the direction of propagation of topographic Rossby waves.

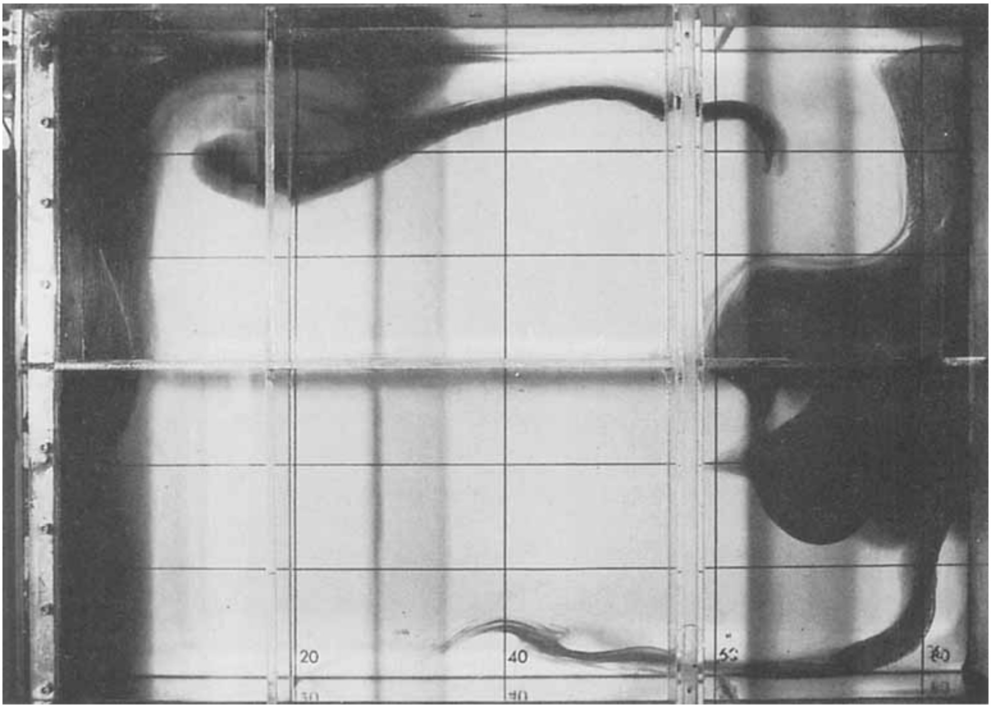

FIGURE 6. Dye streaks of the warm and cold flows observed when the cavity was divided in two ($Ra = 2.4 \times 10^9$, $Ek = 3.6 \times 10^{-5}$ and $Fr = 29$). The cold endwall is on the left, the warm on the right and the centre of rotation is off to the right. The photograph was taken 40 rotation periods after the dye was introduced at both endwalls.

and lid of the cavity were tangent to the potential surfaces (generally $x/L = 0.5$) could be translated by elevating one end of the cavity. Accordingly, the heated endwall of the cavity was elevated by 3 cm. Under these conditions the cyclonic gyre then covered approximately one-fifth of the cavity ($0 < x/L < 0.2$) and the anticyclonic gyre expanded over the remaining area ($0.2 < x/L < 1.0$). The value of $x/L = 0.2$ corresponds to the position where the tangent (of slope 3/200) touches the parabola (equation (6)). Similarly, when the cooled end was elevated, the cyclonic gyre filled the majority of the cavity and the anticyclonic gyre the remainder. Taking this a step further, it was found that provided the slope was greater than $f^2L/8g$, the cavity filled with a cyclonic gyre when the cooled end was elevated and an anticyclonic gyre when the heated end was elevated.

Further evidence of these effects was found during experiments in which a conducting plate was inserted near the centre of the cavity and fluid on one side of the barrier stirred. As well as increasing the aspect ratio, this also offset the centre of the flow from the centre of rotation. When the cooled endwall was near the centre of rotation, a single cyclonic gyre filled the cavity and when the heated endwall was near the centre, an anticyclonic gyre filled the cavity (figure 6). All of these observations confirm that the mean flow was to a large extent controlled by the slope of the potential surfaces relative to the bottom and lid of the cavity.

The relative slope of potential surfaces and horizontal boundaries may also support topographic Rossby waves. Since there are no variations in the total fluid depth, barotropic Rossby waves are excluded. However, trapped baroclinic Rossby waves may propagate near the top and bottom of the cavity in the directions indicated in figure 5. Neglecting the curvature (but not the slope) of the isopotentials, the dispersion relation for these waves is given by

$$\sigma \sim -\frac{\partial \eta}{\partial x}\frac{Bf}{HFr^{\frac{1}{2}}}\sin\varphi \tag{7}$$

(Rhines 1970), where φ is the horizontal angle of the wave vector to the x-axis. The wave amplitude decays exponentially away from both the upper and lower boundary with an e-folding depth of

$$d = HFr^{\frac{1}{2}}/BK \tag{8}$$

(Rhines 1970), where K is the wavenumber. Clearly, baroclinic waves can only propagate when this depth is less than the fluid depth or $K > Fr^{\frac{1}{2}}/B$.

There are two additional factors which restrict the Rossby wave spectrum. The first is the finite length and width of the cavity, which excludes modes with wavelengths greater than $\frac{1}{2}L$. The second is dissipation, which strongly damps modes trapped within the Ekman layers (of depth $HEk^{\frac{1}{2}}$). If we include these factors, Rossby wave behaviour in the cavity can be summarized in the following way: there are no modes with non-dimensional wavenumbers in the range

$$K < \max\left\{\frac{4\pi}{L}, \frac{Fr^{\frac{1}{2}}}{B}\right\} \tag{9}$$

due to finite dimensions of cavity; wavenumbers in the range

$$\max\left\{\frac{4\pi}{L}, \frac{Fr^{\frac{1}{2}}}{B}\right\} < K < \frac{1}{B}\left(\frac{Fr}{Ek}\right)^{\frac{1}{2}} \tag{10}$$

correspond to the trapped modes; and short waves with

$$K > \frac{1}{B}\left(\frac{Fr}{Ek}\right)^{\frac{1}{2}} \tag{11}$$

are rapidly damped out by dissipation. Relation (10) indicates that Rossby waves can propagate provided

$$Ek < \min\left\{\frac{Fr}{16\pi^2}\left(\frac{L}{B}\right)^2, 1\right\}. \tag{12}$$

This condition is satisfied for the entire experimental parameter range; however the waves will only play a significant role in the dynamics of the flow if

$$\frac{\partial \eta}{\partial x} > \frac{d}{\frac{1}{2}L}. \tag{13}$$

This is equivalent to requiring that the horizontal scale of the flow $\frac{1}{2}L$ is greater than the Rhines radius f/β, where $\beta = (f/d)\, \partial\eta/\partial x$. From (6), $\partial\eta/\partial x \sim f^2L/8g$ and using (8), relation (13) becomes

$$K > 16\frac{gH}{f^2L^2}\frac{Fr^{\frac{1}{2}}}{B}. \tag{14}$$

Combining this with result (10) indicates that Rossby waves will only be important if

$$Ek < \left(\frac{\nu^2L^2}{16gH^5}\right)^{\frac{2}{5}}. \tag{15}$$

For our cavity this condition is equivalent to $Ek < 1.6 \times 10^{-4} (f > 0.27)$.

The Rossby wave dynamics may be complicated as a result of distortion of the isopotential surfaces by the flow and additional dissipation by eddy fluxes. However, the arguments presented above suggest that baroclinic Rossby waves may influence the flow in the cavity during experiments with sufficiently small Ekman numbers. The waves should propagate towards most of the boundary currents (1, 3, 4 and 5 in figure 3), tending to transfer energy into these flows and intensify them. In contrast, the warm return flow (current 2) would tend to be dissipated by energy loss to the waves. However, observations of dye streaks, along with potential vorticity data to be presented in §4, indicate that both of the inertial currents (2 and 3) were subsurface flows and thus may not have been affected by waves trapped near the horizontal boundaries.

4. The temperature and potential vorticity fields

With an understanding of the basic dynamics of the cavity flow, we can now continue with a detailed description of properties such as the temperature and potential vorticity fields. Temperature sections were recorded at approximately 20 minute intervals after the flow had been allowed to develop to a steady mean state. These data were averaged over time in order to remove the fluctuating signal due to individual eddies and thus obtain a mean temperature field. Alternatively, the variability associated with eddies was determined by calculating the standard deviation of temperature from the mean, at each point in the cross-section. The temperature data were also used to determine the potential vorticity distribution, which is both a dynamically important property and a conserved tracer in the absence of dissipation at boundaries (see the review by Rhines 1986). The role of potential vorticity in revealing the structure of ocean circulation is well established (Talley 1988). In this paper it will be shown that, under certain circumstances, it can be equally useful in the laboratory.

The potential vorticity q is defined as

$$q = \frac{(\boldsymbol{f}+\boldsymbol{\zeta})\cdot\boldsymbol{\nabla}\rho}{\rho}, \tag{16}$$

where $\boldsymbol{\zeta} = \boldsymbol{\nabla} \times \boldsymbol{u}$ is the relative vorticity and ρ is a conservative fluid property,

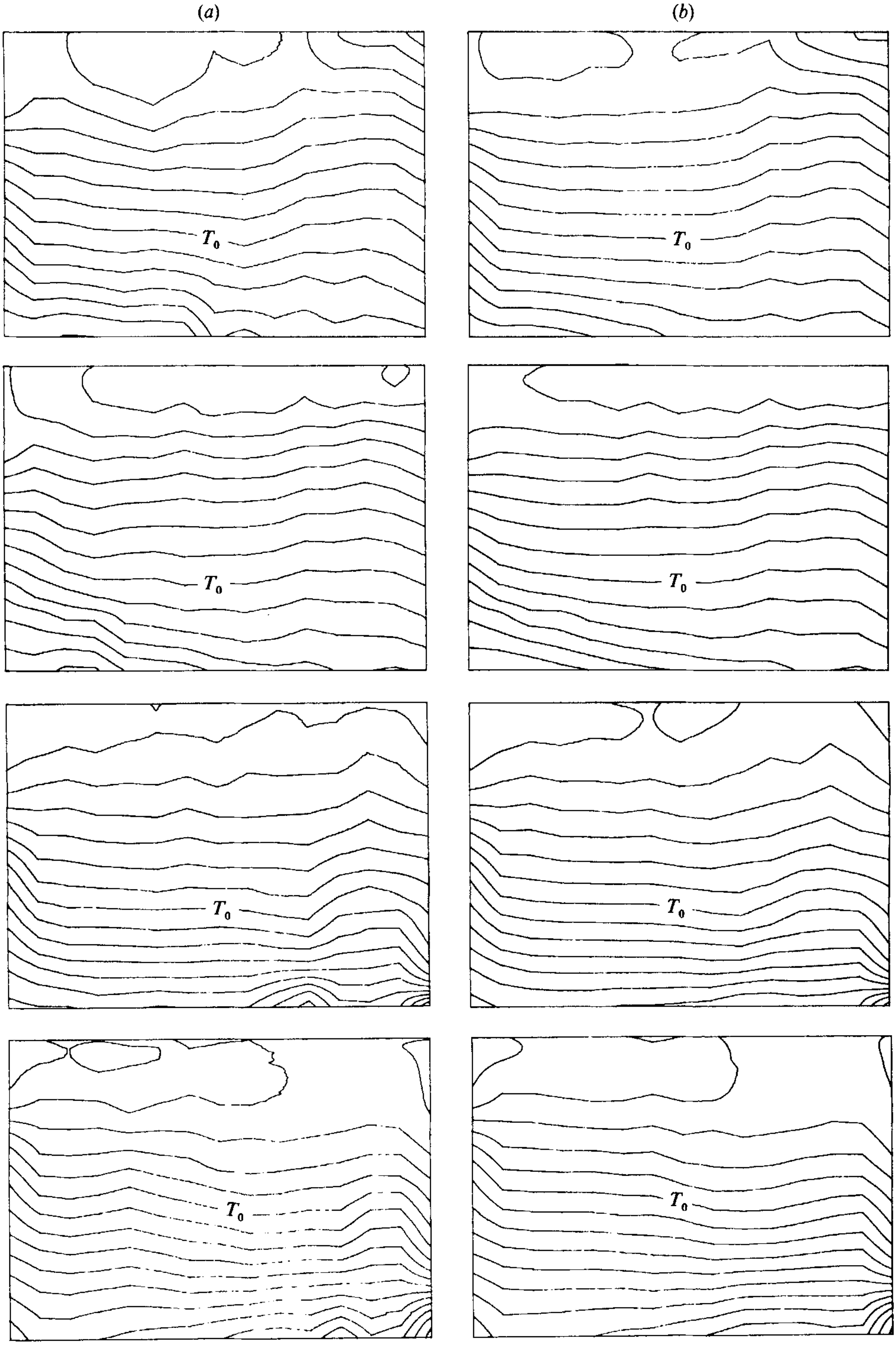

FIGURE 7 (*a*, *b*). For caption see page 464.

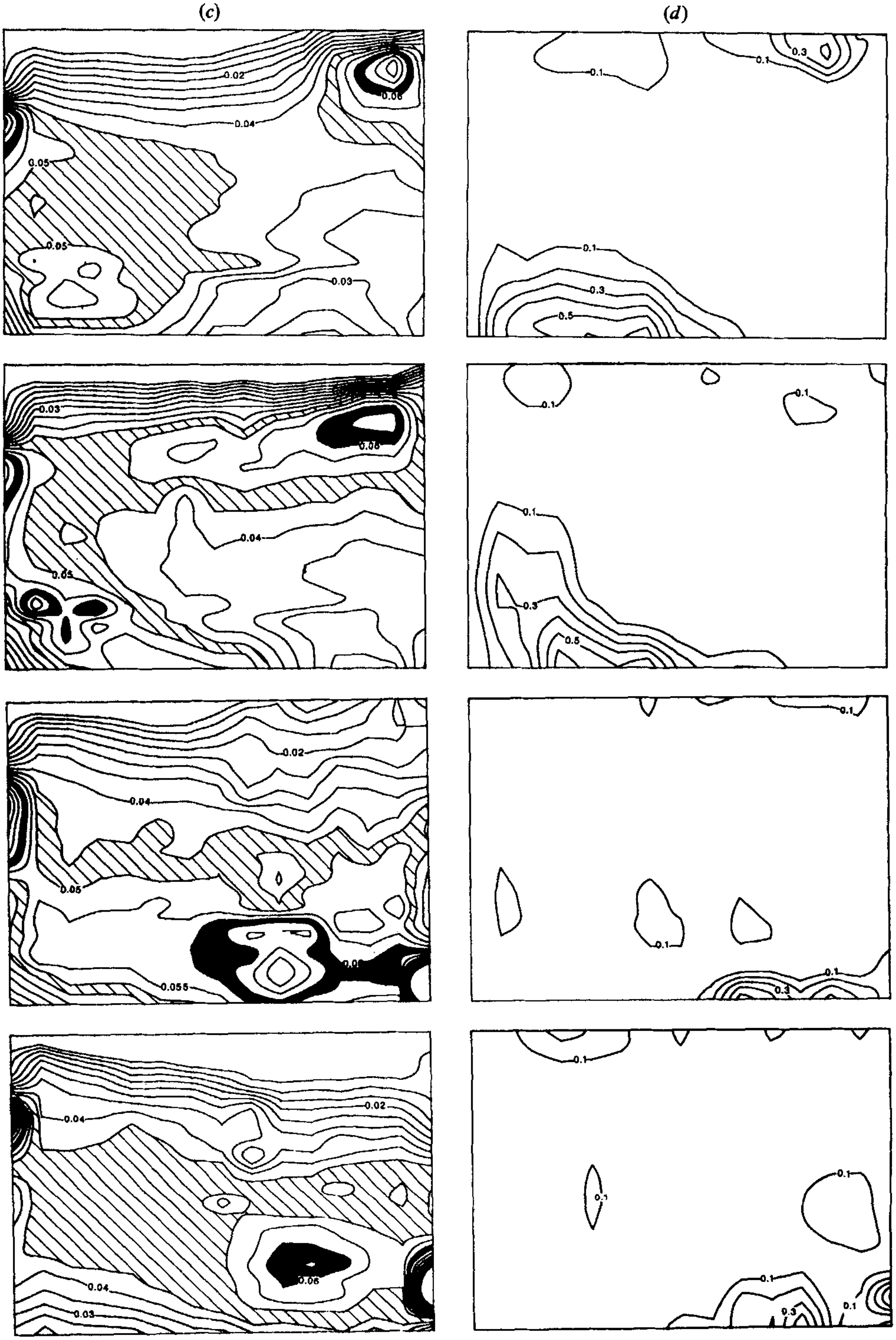

FIGURE 7 (*c*, *d*). For caption see page 464.

usually the fluid density. Assuming that the vertical velocities are negligible, (16) can be expanded to give

$$q = \frac{1}{\rho}\left(\frac{\partial u}{\partial z}\frac{\partial \rho}{\partial y} - \frac{\partial v}{\partial z}\frac{\partial \rho}{\partial x} + (f+\zeta)\frac{\partial \rho}{\partial z}\right), \tag{17}$$

where $\zeta = (\partial v/\partial x) - (\partial u/\partial y)$ is the vertical component of the relative vorticity. For the experimental parameter range, the vertical stratification was sufficiently large and the vertical gradients of horizontal velocities (determined from velocity profiles such as those in figure 4) sufficiently weak, that

$$\frac{\partial u}{\partial y}\frac{\partial \rho}{\partial z} \sim \frac{\partial v}{\partial x}\frac{\partial \rho}{\partial z} > \frac{\partial u}{\partial z}\frac{\partial \rho}{\partial y} > \frac{\partial v}{\partial z}\frac{\partial \rho}{\partial x}.$$

Furthermore, $\zeta/f < 10^{-1}$, even in the regions of maximum horizontal shear. Equation (17) can therefore be approximated by

$$q = \frac{f}{\rho}\frac{\partial \rho}{\partial z}. \tag{18}$$

Since the density stratification in the convection experiment was produced solely by temperature variations, (18) can be written in the form

$$q = f\alpha\frac{\partial T}{\partial z}, \tag{19}$$

where the coefficient of thermal expansion α is a function of temperature. Hence, calculation of the potential vorticity field required only measurements of the temperature and vertical temperature gradient. In regions where diffusion, viscous dissipation and forcing are all negligible, fluid elements conserve their potential vorticity and we can write, $\mathrm{D}/\mathrm{D}t(\alpha\,\partial T/\partial z) = 0$.

Figure 7 illustrates the flow characteristics described above at four different cross-sections in the cavity under a single set of conditions. The first column of contour plots (figure 7*a*) are examples of the instantaneous temperature fields at the various cross-sections. While the temperature gradients were nonlinear, the density gradients ($\rho_0\,\alpha\,\partial T/\partial z$) were nearly linear over most of the cross-section. Some heat loss through the cavity lid is evident; however, the profiles do not extend close enough to the bottom to detect any change through this surface. The signature of individual eddies can sometimes be distinguished in these profiles by comparing them with the time-averaged temperature profiles in the second column (figure 7*b*). The latter were produced by averaging the temperature at each point over ten profiles, taken over a period of approximately four hours (equivalent to from 100 to 2000 rotation periods for the range of rotation speeds investigated). The results are consistent with the dye streaks in figure 2 and the sketch in figure 3, with the crossing of the warm

---

FIGURE 7. Profiles of various flow characteristics at $x/L = 0.28$, 0.43, 0.65 and 0.80 respectively (moving from the top to the bottom of the page) when $Ra = 2.2\times10^9$, $Ek = 2.4\times10^{-5}$ and $Fr = 71$. The profiles cover the cross-sections to within 0.5 cm of the side and bottom boundaries and completely to the top of the cavity. The conditions are the same as those in figure 1. (*a*) Examples of the instantaneous temperature profiles. T_0 is the average of the endwall temperatures and the isotherms are at 1.0 °C intervals. (*b*) The temporally averaged temperature profiles. (*c*) Potential vorticity profiles. Isolines of potential vorticity are at intervals of 0.005 $\mathrm{m^{-1}\,s^{-1}}$ and the shading corresponds to 0.045–0.050 $\mathrm{m^{-1}\,s^{-1}}$ for the lighter regions and 0.060–0.065 $\mathrm{m^{-1}\,s^{-1}}$ for the dark regions. (*d*) Contours of constant standard deviation in temperature at 0.1 °C intervals.

flow from the right- to the left-hand side boundary particularly well defined by the cross-cavity slopes of the isotherms. Efficient lateral mixing by eddy motions ensured that the slope of isotherms was generally small in regions away from the strong boundary currents.

Column (*c*) in figure 7 shows the potential vorticity fields calculated by applying (19) to the temporally averaged temperature values. This is undoubtedly the most revealing form in which to present the temperature data. It reveals the strong currents, as regions of high potential vorticity, flowing away from the heated and cooled endwalls much more clearly than does the raw temperature field. Furthermore, the conservation of potential vorticity (except for dissipation at boundaries and creation at the endwalls) allows mean fluid paths to be followed from one profile to the next. In figure 7 some of the regions of equal potential vorticity are shaded to allow paths to be easily traced. Broadening of the warm current (top right-hand corner of the profiles and current 1 in figure 3) with distance from the hot wall is clearly marked. This region of the flow also demonstrates the horizontal diffusion of q by eddy motions, and its dissipation within the Ekman layers. In particular, the magnitude of the potential vorticity decayed with distance from the source, while the depth at which the maximum value occurred increased. Some of these aspects are even more distinct in the cold region of the flows. Working from the bottom to the top of figure 7 (*c*), the cold current (current 4 in figure 3) widened, then crossed to the opposite side boundary where it progressed towards the heated endwall (as current 5). There was significant dissipation over this path; however, the basic shape of the current was preserved.

Another prominent feature of all the potential vorticity profiles is a concentration of q approximately two-thirds of the way up the left-hand boundary (some evidence of this can also be seen in the raw temperature profiles). This feature corresponds to the two jets (2 and 3 in figure 3) which carried warm fluid away from the central region of the tank, towards the two endwalls as described in §2. The depth of the currents, and their strong confinement to the side boundary, suggests that they are inertial rather than driven by buoyancy. The portion of this flow which returned to the heated endwall as part of the cyclonic gyre did not appear to have a distinct counterpart in the cold flow. As discussed in §3, this asymmetry may have resulted from nonlinearity in the equation of state for water and the consequent difference in buoyancy fluxes out of the two endwall regions.

The cold current near the cooled endwall (bottom right-hand corner of the last two profiles in column *c*) had a particularly complex potential vorticity structure. This may have been related to the opposing influences of the linear Coriolis term in the momentum equation and the nonlinear potential vorticity constraints. The resulting current appeared to consist of two interacting components. One component was centred against the sidewall and had similar characteristics to the inertial currents discussed above. The other component was centred some distance from the sidewall and resembled the warm current at the other end of the cavity. Since the potential vorticity of the latter component increased with distance from the source, there must have been significant input of fluid from the inertial component which had greater potential vorticity.

In regions away from the boundaries and strong currents, the potential vorticity gradients were generally small. This is particularly true of the first and last profiles in figure 7 (*c*) which correspond to the central regions of the large-scale gyres. It is suggested that these cross-sections may reveal islands of nearly constant q covering the central area of the gyres. Within such islands, dissipation is small and time-mean

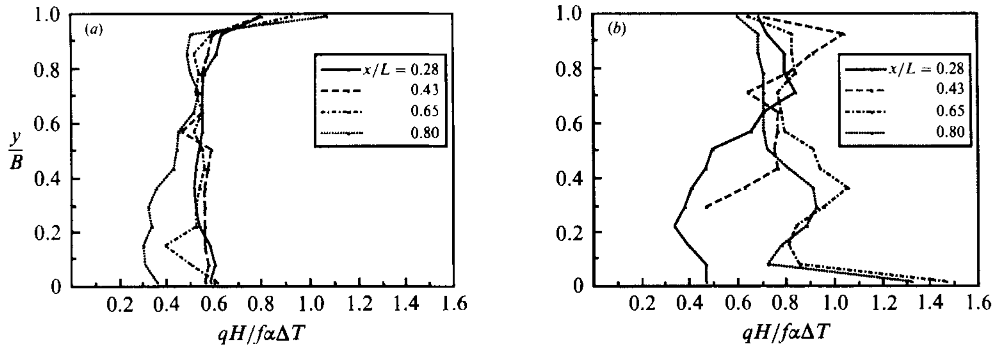

FIGURE 8. The non-dimensional vorticity distribution measured along the isotherms (*a*) $T_0+\frac{1}{8}\Delta T$ and (*b*) $T_0-\frac{1}{8}\Delta T$ at the four cross-sections given in figure 7. The applied conditions are also the same as those in figure 7.

streamlines form closed loops. Potential vorticity gradients are expelled from these regions and eddy stirring maintains a homogeneous distribution of q. The degree of homogenization depends on the relative magnitudes of the diffusive timescale and the timescale over which the stream function varies (Rhines & Young 1983). Observations in the cavity indicate that the stream function associated with the mean flow was independent of time (as were the boundary conditions), suggesting that conditions may have been suitable for significant homogenization.

Since both density and potential vorticity are conserved along streamlines in the absence of diffusion and dissipation, it is useful to replot the potential vorticity distribution along isotherms. Figure 8 shows the results for two isotherms using the same data as those used to produce figure 7. The isotherms have been chosen to include most of the strong currents, while generally excluding the Ekman layers where dissipation dominates. As in the contour plots of figure 7, regions of relatively strong flow and regions dominated by eddy stirring are clearly distinguishable. One clear advantage of plotting the data along density surfaces is that, if we follow the distribution of q from one section to the next, we find that conservation of potential vorticity demands that the flow field be like that depicted in figure 3. In particular, with the exception of the signal associated with the inertial return flow, the potential vorticity maxima swaps to the opposite side of the cavity for both isotherms near $x/L = 0.5$.

Column (*d*) in figure 7 illustrates the distribution of variability associated with the turbulent eddy field in the cavity. Contours of constant standard deviation in temperature calculated from the ten profiles are shown. As might be expected, regions of high variability are correlated with the position of strong currents where large vertical and horizontal shears lead to instability. The maximum variability occurred near the horizontal boundaries, but probably outside the Ekman layers. The two inertial jets on the left-hand wall which carried warm fluid from the centre of the cavity to the two endwalls showed less variability. This result is consistent with the dye observations which indicated that these currents were more stable. The variability associated with the cold current in the two sections closest to the cooled end, supports the earlier assertion that this part of the flow consisted of two components. Generally, as eddies moved away from the regions of baroclinic instability, their vorticity was dissipated by Ekman-layer pumping and the level of variability decayed.

5. *Ek*, *Fr* and *Ra* dependence

The general circulation of the ocean is determined by the forcing of wind and buoyancy, the size of the ocean basin, dissipation at boundaries and internal mixing of buoyancy and momentum. Analogous features exist in the convection experiment and each can be represented by one of the parameters defined in §2. For example, the size of the basin is described by the Froude number, which is the ratio of the width of the cavity to the Rossby deformation radius, while the role of dissipation is determined by the Ekman number. Both of these parameters were varied by changing the rotation rate. The Rayleigh number, on the other hand, describes the strength of the forcing and is controlled experimentally by the applied temperature difference.

A single cross-section ($x/L = 0.28$) has been used to illustrate the dependence of the temperature, potential vorticity and variability, on the Froude and Ekman numbers (figure 9). The average temperature profiles (column *a*) indicate that the vertical temperature gradients were almost independent of rotation over most of the cross-section. The cross-stream temperature gradients were smaller at low Froude numbers, as would be expected for a geostrophic flow. However, even at large Froude numbers, lateral transport by eddy motions significantly reduced the slope of isotherms outside the strong current regions. The temperature profiles also indicated that, with an increase in Froude number, the width of the strong boundary currents was reduced while the depth was increased.

The dimensions of the strong currents were more clearly defined by the potential vorticity fields (figure 9*b*). These profiles also indicate that, while the total potential vorticity of the flow increased with Froude number, the basic character of the flow is preserved over the parameter range. In fact, the maximum q of the strong currents is directly proportional to the rotation rate. This result is consistent with (19), since the vertical temperature gradient was almost independent of f. Comparisons with profiles at other cross-sections (not shown) point to an increased rate (per unit time) of dissipation of potential vorticity as the Ekman number is reduced. This is principally the result of a faster 'spin-down' through dissipation within the Ekman layers.

The standard deviation contours in figure 9(*c*) are again correlated with regions of strong flow. Although the spatial distribution of temperature variability is Froude-number dependent, the magnitude of variability generally is not. Notable exceptions to this are when $Ek > 10^{-4}$ or $Fr \lesssim 1$. Condie & Ivey (1988) pointed out that the condition $Ek > 10^{-4}$ is satisfied when the timescale for the growth of waves (~ 10 rotation periods) exceeds the spin-down time for fluid columns ($\tau \sim H(\frac{1}{2}\nu f)^{-\frac{1}{2}}$). Waves therefore failed to break and variability was small. When $Fr \ll 1$, shallow currents covered the entire width of the cavity and were stable. At slightly higher Froude numbers ($Fr \sim 1$) eddies formed; however, the dimensions, location and interactions of eddies were strongly influenced by the side boundaries. Hence the variability associated with processes such as advection and interaction of eddies was almost absent.

The other parameter varied during the experiments was the Rayleigh number, although technical limitations restricted variation in *Ra* to a factor of 3.6. This was the dominant parameter in determining the stratification in the cavity. Away from the endwall boundary layers and the boundary currents, the vertical temperature gradient was relatively constant over the cavity. Measurements along the centre of the tank ($y = 30$ cm) over the full parameter range investigated gave $\partial T/\partial z =$

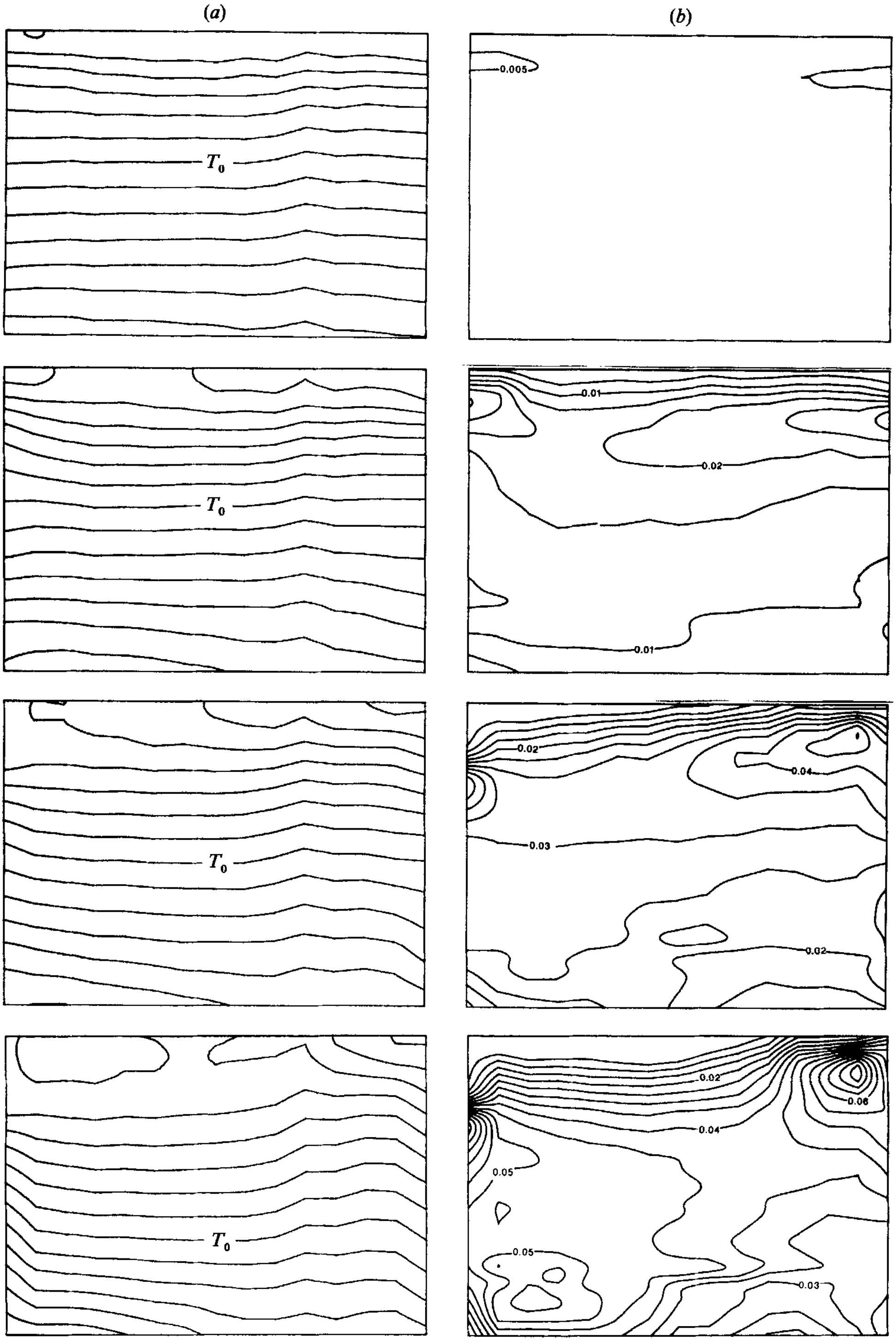

FIGURE 9(*a*, *b*). For caption see facing page.

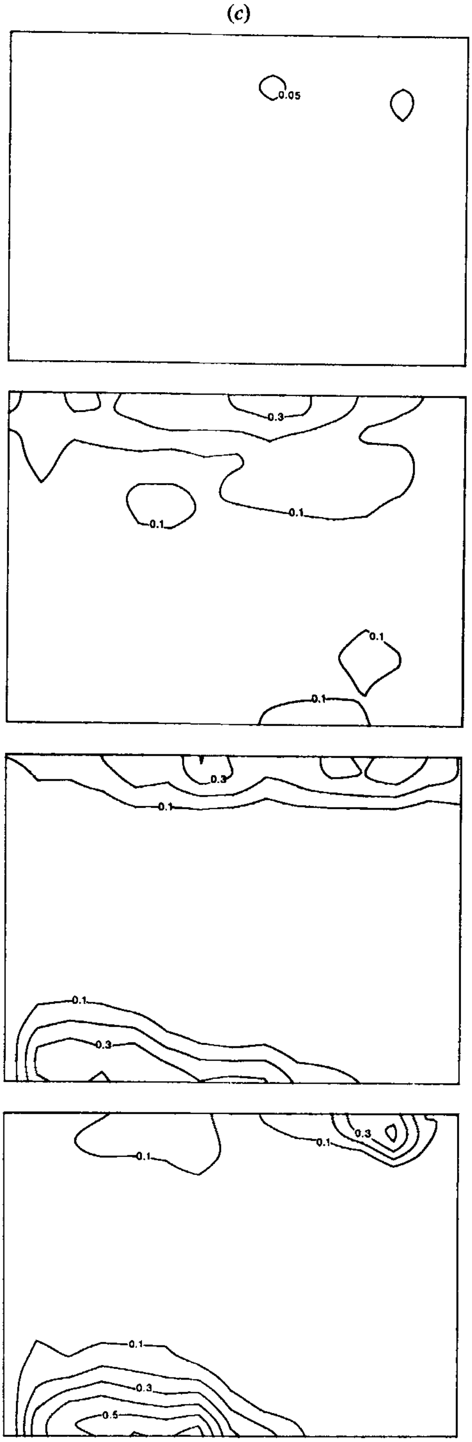

FIGURE 9. (*a*) Averaged temperature, (*b*) potential vorticity, and (*c*) standard deviation in temperature at a single cross-section ($x/L = 0.28$) for a range of rotation rates. The top row corresponds to $Ek = 3.6 \times 10^{-4}$, $Fr = 0.33$, the second row to $Ek = 7.1 \times 10^{-5}$, $Fr = 8.3$, the third row to $Ek = 3.6 \times 10^{-5}$, $Fr = 33$ and the last row to $Ek = 2.4 \times 10^{-5}$ and $Fr = 71$. In all cases $Ra = 2.1 \times 10^{9}$.

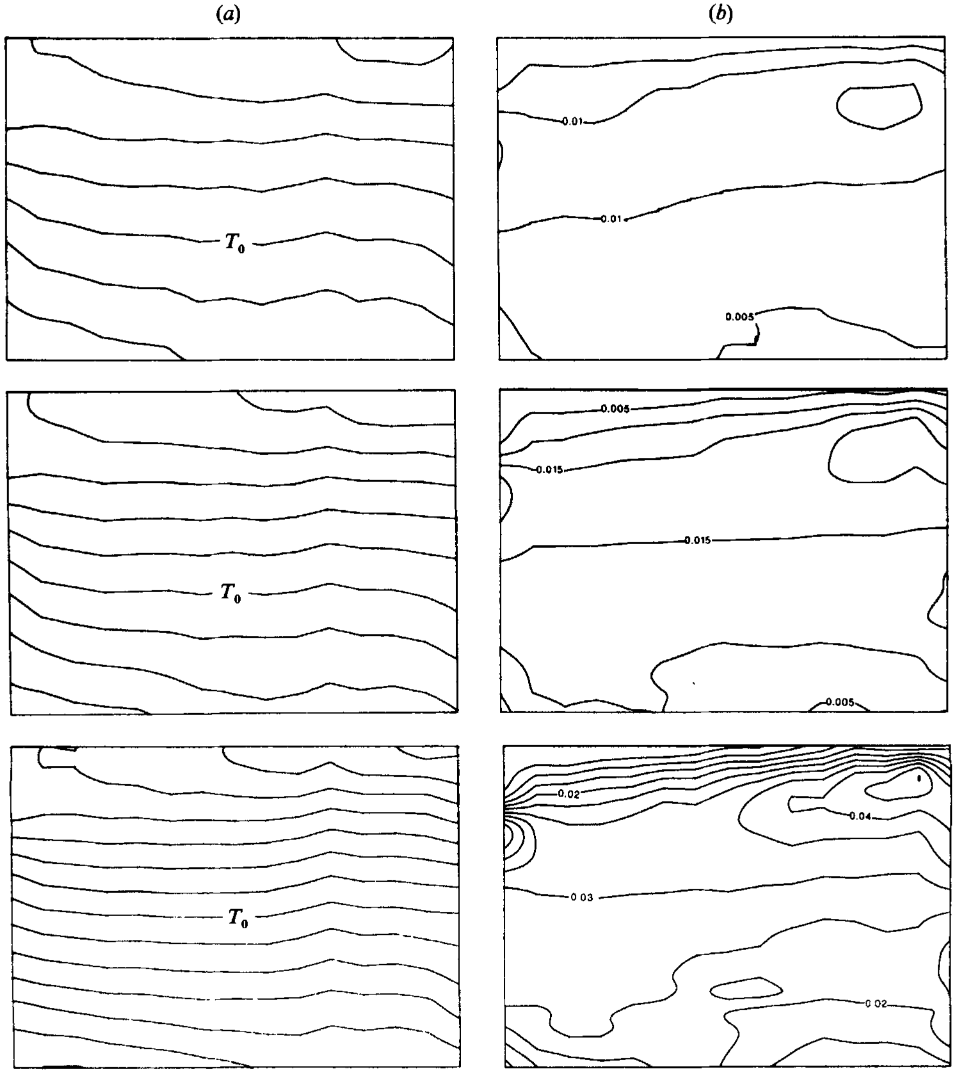

FIGURE 10(*a*, *b*). For caption see facing page.

$(0.55 \pm 0.04)\,\Delta T/H$. Figure 10 demonstrates the Rayleigh-number dependence for the same cross-section ($x/L = 0.28$) as that used in the previous comparisons. The potential vorticity contours indicate that the width of the strong current regions may increase slightly with *Ra*, consistent with the dependence of the deformation radius on $\Delta T^{\frac{1}{2}}$. More importantly, as the Rayleigh number is increased, larger potential vorticity gradients reflect an increase in the strength of the flow. The last column (*c*) shows the dependence of the standard deviation of temperature on Rayleigh number. The increase in temperature variability with *Ra* results from the larger horizontal temperature gradients within the flow and, to a lesser extent, the more unstable nature of the flow.

The above series of experiments demonstrated the role played by varying each of the parameters (apart from the aspect ratio and Prandtl number). The Froude number determined the lengthscales of the flow, with both the density and velocity fields giving lengthscales which varied significantly over the parameter range

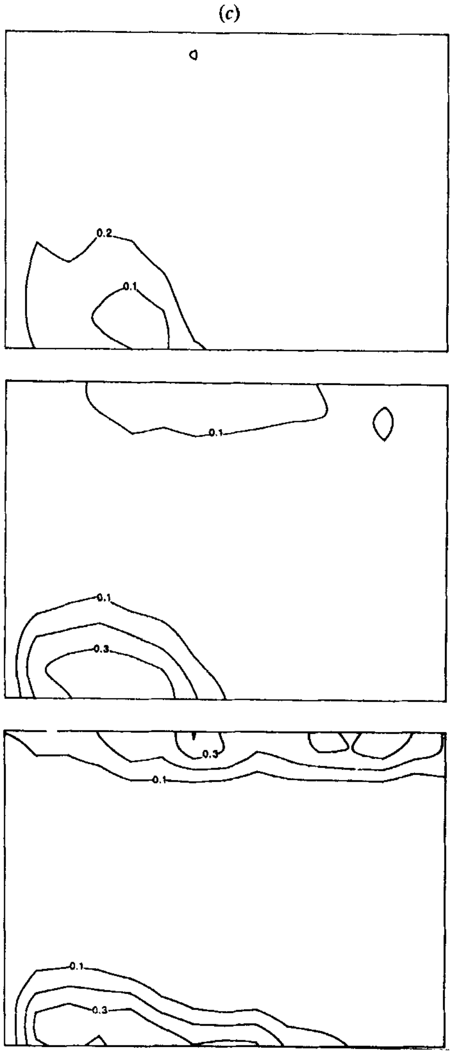

FIGURE 10. (*a*) Averaged temperature, (*b*) potential vorticity, and (*c*) standard deviation in temperature at a single cross-section ($x/L = 0.28$) for a range of applied temperature differences. The three rows correspond to $Ra = 5.8 \times 10^8$, 8.7×10^8 and 2.1×10^9 respectively. In each case $Ek = 4 \times 10^{-5}$.

investigated. The Ekman number described the dissipation in the flow and therefore determined whether waves broke to form eddies. The magnitude of density gradients and flow velocities were functions of the endwall forcing and were therefore determined by the Rayleigh number.

6. Heat transfer

The total heat transport by the fluid is a fundamental quantity in all studies of free convection. It is particularly important in the ocean in relation to climate studies, since the ocean is thought to be responsible for approximately half the net heat transfer between equatorial and polar regions. The experiment was accordingly designed to allow for measurement of the longitudinal heat transfer. The two

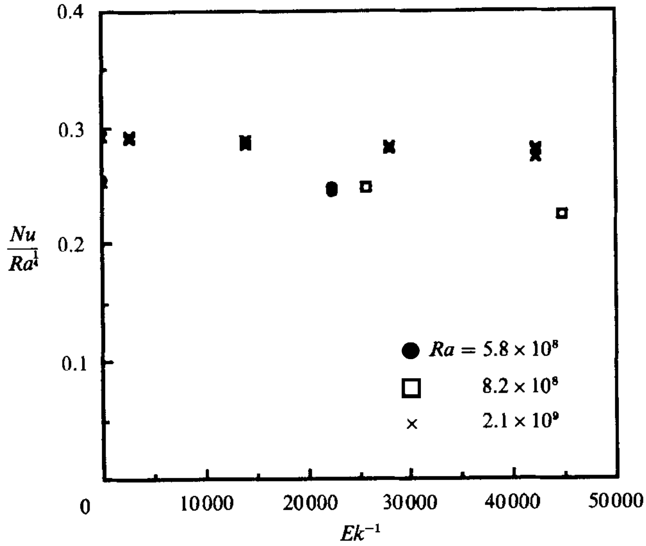

FIGURE 11. The Nusselt number divided by $Ra^{\frac{1}{4}}$ as a function of inverse Ekman number for a range of Rayleigh numbers.

endwalls of the cavity consisted of an aluminium plate (through which the heated or cooled fluid flowed) connected to a copper plate which was in contact with the working fluid. Thermistors embedded in the aluminium and copper allowed the temperature gradient between the two plates to be measured. Once the system was calibrated, the thermistor readings could be used to calculate the heat transfer through each endwall.

The heat flux through the hot endwall was generally found to be a few percent higher than that through the cold end due to a small net heat loss. The heat transfer through the hot end over a range of Ekman and Rayleigh numbers is presented in figure 11. It is expressed in the form of a Nusselt number (ratio of the total heat transfer to the conductive component of the heat transfer) divided by $Ra^{\frac{1}{4}}$, which is the predicted Rayleigh-number dependence for the non-rotating case (Patterson & Imberger 1980). The heat flux is found to be weakly dependent on rotation with a slight increase in Nusselt number with Ekman number (decreasing rotation rate). This may be due to the more rapid dissipation of momentum within the Ekman layers or the more unstable nature of the mean flow at small Ekman numbers. Another factor which may have influenced the heat flux was the parabolic distortion of potential surfaces associated with rotation. Fluid emerging from the base of the cold endwall would need to cross isopotentials in order to reach the centre of the cavity and this would tend to impede the flow of heat and mass between the endwalls. The important result from these measurements is that the effects of rotation on the heat transfer were secondary when compared to the Rayleigh-number dependence.

7. Relevance to ocean circulation

The mean flow observed in the cavity differs substantially from that expected on the basis of Kelvin wave dynamics. This has been explained largely in terms of the potential vorticity dynamics and the parabolic shape of isopotential surfaces. The experiments are therefore of some relevance to oceanic flows over topography on scales of a few hundred kilometres, since the effects of bottom slope are then much larger than the β-effect (Rhines 1969). Documented examples include the overflow from the Denmark Straits, the large-scale mean bottom circulation of the western North Atlantic (Tucholke, Wright & Hollister 1973), flow over the mid-Atlantic ridge (Fu, Keffer & Wunsch 1982) and the deep flow in Drake Passage (Rattray 1985).

The dynamics of the experiment also suggest an analogy with ocean circulation on a β-plane. While the exact dynamical equivalence between a sloping bottom with constant Coriolis parameter f and a variation in f with latitude (the β-effect) does not strictly hold for stratified flows, a useful similarity between the two systems exists for some aspects of the flow. The predicted propagation of baroclinic Rossby waves towards most of the major currents points to an analogy with baroclinic western boundary currents in the oceans. However, it is generally accepted that western currents are inertial flows responding to the wind-driven circulation, while the laboratory currents are buoyancy flows which may be modified by Rossby waves. The laboratory currents probably have more in common with surface gravity currents such as the East Greenland Current (Wadhams, Gill & Linden 1979), the Norwegian Coastal Current (Mysak & Schott 1977) and the Alaska Coastal Current (Ahlnas, Royer & George 1987).

It was noted in §3 that only the warm current returning towards the heated endwall of the cavity might loose energy to Rossby waves in the manner of an eastern boundary current on a β-plane. However, both of the warm inertial currents on the left-hand wall (currents 2 and 3 in figure 3) were some distance below the lid and therefore may not have been significantly influenced by either Rossby wave propagation or the relative slope of the lid and potential surfaces. There are oceanic flows which similarly impinge on a coastline and break into oppositely directed boundary jets. One example of this is the formation of boundary jets in the Alboran Sea from flow impinging on the African coast (Whitehead & Miller 1979).

The experiments encompassed a number of other important aspects of thermohaline circulation in large-scale water bodies. The effects of forcing, dissipation and basin size on flow characteristics such as the velocity field, stratification, variability and potential vorticity distribution have been examined. The potential vorticity is the dynamically important quantity which governs the motions and, as in the oceans (Talley 1988), has been particularly useful in revealing the structure of the mean flow in the laboratory cavity. Furthermore, the strong correlation in every detail between the flow field traced by the dye streaks and that indicated by the potential vorticity field clearly demonstrates the validity of using the potential vorticity as a tracer for the flow. It is evident that the potential vorticity distribution yields much more information than the raw density data and it may play an important role in future laboratory studies on rotating stratified fluids.

Derek Corrigan, Pat Travers, Ross Wylde-Browne and Tony Beasley are thanked for technical assistance and advice, as is Dr Roger Nokes who wrote the data logging and plotting routines.

REFERENCES

AHLNAS, K., ROYER, T. C. & GEORGE, T. H. 1987 Multiple dipole eddies in the Alaska coastal current detected with Landsat thermatic mapper data. *J. Geophys. Res.* **92**, 13041–13047.

BEJAN, A., AL-HOMOUD, A. A. & IMBERGER, J. 1981 Experimental study of high-Rayleigh-number convection in a horizontal cavity with different end temperatures. *J. Fluid Mech.* **109**, 283–299.

CONDIE, S. A. 1989 A laboratory model of a convectively driven ocean. *Dyn. Atmos. Oceans* **13**, 77–94.

CONDIE, S. A. & IVEY, G. N. 1988 Convectively driven coastal currents in a rotating basin. *J. Mar. Res.* **46**, 473–494.

CORMACK, D. E., LEAL, L. G. & IMBERGER, J. 1974 Natural convection in a shallow cavity with differentially heated end walls. Part 1. Asymptotic theory. *J. Fluid Mech.* **65**, 209–229.

FU, L.-L., KEFFER, P. P. & WUNSCH, C. 1982 Observations of mesoscale variability in the western North Atlantic: a comparative study. *J. Mar. Res.* **40**, 809–848.

IMBERGER, J. 1974 Natural convection in a shallow cavity with differentially heated end walls. Part 3. Experimental results. *J. Fluid Mech.* **65**, 247–260.

MYSAK, L. A. & SCHOTT, F. 1977 Evidence for baroclinic instability off the Norwegian Current. *J. Geophys. Res.* **82**, 2087–2095.

PATTERSON, J. C. 1984 Unsteady natural convection in a cavity with internal heating and cooling. *J. Fluid Mech.* **140**, 135–151.

PATTERSON, J. C. & IMBERGER, J. 1980 Unsteady natural convection in a rectangular cavity. *J. Fluid Mech.* **100**, 65–86.

PEDLOSKY, J. 1979 *Geophysical Fluid Dynamics*. Springer.

RATTRAY, M. 1985 The effect of bathymetry on the deep flow in Drake Passage. *Deep-Sea Res.* **32**, 127–147.

RHINES, P. B. 1969 Slow oscillations in an ocean of varying depth. Part 1. Abrupt topography. *J. Fluid Mech.* **37**, 161–189.

RHINES, P. B. 1970 Edge-, bottom-, and Rossby-waves in a rotating stratified fluid. *Geophys. Fluid Dyn.* **1**, 273–302.

RHINES, P. B. 1986 Vorticity dynamics of the ocean general circulation. *Ann. Rev. Fluid Mech.* **18**, 433–497.

RHINES, P. B. & YOUNG, W. R. 1983 How rapidly is a passive scalar mixed within closed streamlines. *J. Fluid Mech.* **133**, 133–145.

SIMPKINS, P. G. & DUDDERAR, T. D. 1981 Convection in rectangular cavities with differentially heated end walls. *J. Fluid Mech.* **110**, 433–456.

SPEER, K. G. & WHITEHEAD, J. A. 1989 A gyre in a non-uniformly heated rotating fluid. *Deep-Sea Res.* (in press).

SUGIMOTO, T. & WHITEHEAD, J. A. 1983 Laboratory models of bay-type continental shelves in the winter. *J. Phys. Oceanogr.* **13**, 1819–1828.

TALLEY, L. D. 1988 Potential vorticity distribution in the North Pacific. *J. Phys. Oceanogr.* **18**, 89–106.

TUCHOLKE, B. E., WRIGHT, W. R. & HOLLISTER, C. D. 1973 Abyssal circulation over the Greater Antilles Ridge. *Deep-Sea Res.* **20**, 973–995.

WADHAMS, P., GILL, A. E. & LINDEN, P. F. 1979 Transects by submarine of the East Greenland Polar Front. *Deep-Sea Res.* **26A**, 1311–1327.

WHITEHEAD, J. A. & MILLER, A. R. 1979 Laboratory simulation of the gyre in the Alboran Sea. *J. Geophys. Res.* **84**, 3733–3742.